# Supplementary Materials for

## Four-dimensional imaging of carrier interface dynamics in p-n junctions

Ebrahim Najafi, Timothy D. Scarborough, Jau Tang, Ahmed Zewail*

*Corresponding author. E-mail: zewail@caltech.edu

Published 9 January 2015, *Science* **347**, 164 (2015)
DOI: 10.1126/science.aaa0217

**This PDF file includes:**



**Other Supplementary Material for this manuscript includes the following:**
(available at www.sciencemag.org/cgi/content/full/347/6218/164/DC1)

## Materials and Methods

For the silicon p-n junctions investigated in this paper, we estimated the potential barrier and the depletion layer width to be 0.79 eV and 3.29 μm, respectively. If the bandgap narrows from its value by up to 60 meV in p-type due to the high doping level, these calculated values are only slightly changed (*20*). The schematic of the electronic bands in the p-n junction is provided in fig. S1. Since the electric field is only nonzero within the depletion layer, the drift of excited carriers between p-type and n-type is expected only in this region.

Since carrier diffusion in semiconductors can be significantly altered by surface roughness, we only selected samples with the rms roughness of less than 100 nm (orders of magnitude smaller than the estimated diffusion length in silicon (*21*)) for dynamic studies. This was achieved by comparing SUEM images with atomic force microscopy (AFM) images on standard samples to find a qualitative correlation between the SE signal and the actual surface roughness. Figure S2 shows low (A) and high (B) magnification SUEM images (recorded in the static mode, i.e., without time resolution) of a typical sample investigated in this paper. Visually, such surfaces exhibit mirror-like reflection, similar to wafers with polished surfaces.

Figure S3A shows the "raw" SUEM image of the junction prior to laser illumination (negative time at -680 ps). As discussed in the manuscript, the relative contrast between n-type and p-type is due to their different effective electron affinities, resulting from their different doping levels and surface characteristics. The dotted ellipse shows the location of the laser beam at the junction. Figure S3B shows the processed SUEM image of the same region 80 ps after laser excitation; the dynamic signal appears as bright and dark contrasts, corresponding to increased electron and hole densities, respectively. The image processing was carried out as follows. First,

for each time delay, several images were recorded which were then normalized to their background intensities and then averaged to enhance their signal-to-noise ratio. From these images, the reference image (processed similarly) recorded at far negative time was subtracted to remove the static background. As a result, the contrast images reflect changes on the surface relative to negative time. Depending on the sample, the dynamic signal was estimated to be at most 2% of the overall signal in the image and therefore careful processing was needed to enhance it.

**Supplementary Text**

Modeling dynamic carrier density and electric potential

Upon photoexcitation of the p-n junction by a laser pulse, electron-hole (e-h) pairs are generated in the illuminated region with ≈1.3 eV in excess energy. These carriers establish thermal equilibrium amongst themselves within a few hundred femtoseconds at a temperature close to $10^4$ K, and expand ballistically in all directions close to $10^6$ m/s. The presence of the intrinsic electric field inside the depletion layer induces charge gating effects for the carriers which allows the minority carriers to cross the junction while blocking the majority carriers. For example, holes initially excited in p-type with a velocity component travelling toward the junction will encounter the barrier and be reflected, whereas electrons with similar velocity components are transported into n-type. Carriers travelling away from the junction remain unaffected.

Here, we first consider the e-h cloud excited in p-type, and for now neglect the acceleration/deceleration at the junction, which we treat later. The initial carrier density distribution is close to the spatial distribution of the laser power profile with a rms $\sigma \approx 20$ μm. Because the electrons and holes in silicon have a different effective masses, $m_e^*/m_e = 0.26$ and $m_h^*/m_e = 0.386$, respectively, the expansion rates are different. For example, at $10^4$ K, the averaged

thermal velocities for electrons and hole are given by $v_e$ = 0.76 μm/ps and $v_h$ = 0.63 μm/ps, respectively. Assuming a Gaussian e-h cloud distribution (truncated by the junction) upon excitation, the initial density distributions for the p-type and the n-type, respectively, are

$$\rho_{e,h}^{p}(x,y) = \frac{N_p}{\pi\sigma^2}\exp\left(-\frac{x^2+y^2}{2\sigma^2}\right)\eta(-x) \tag{S1}$$

$$\rho_{e,h}^{n}(x,y) = \frac{N_n}{\pi\sigma^2}\exp\left(-\frac{x^2+y^2}{2\sigma^2}\right)\eta(x) \tag{S2}$$

where $\eta$ is the Heaviside step function, and $N_p$ and $N_n$ are the total number of the e-h pairs in p-type and n-type, respectively. For carriers at temperature $T$, the velocities are given by the Maxwell-Boltzmann distribution as

$$f_e(v_x,v_y) = \frac{m_e^*}{2\pi k_B T}\exp\left(-\frac{{v_x}^2+{v_y}^2}{2k_B T}m_e^*\right) \tag{S3}$$

$$f_h(v_x,v_y) = \frac{m_h^*}{2\pi k_B T}\exp\left(-\frac{{v_x}^2+{v_y}^2}{2k_B T}m_h^*\right). \tag{S4}$$

Integrating over the range of velocities gives their distribution $\rho_e^p(x,y;t)$ in space and time:

$$\begin{aligned}\rho_e^p(x,y;t) &= \int_{-\infty}^{\infty} dv_x \int_{-\infty}^{\infty} dv_y\, f_e(v_x,v_y)\rho_e^p(x-v_x t, y-v_y t) \\ &= \frac{N_p}{2\pi\left(\sigma^2+{v_e}^2t^2\right)}\exp\left(-\frac{x^2+y^2}{2\left(\sigma^2+{v_e}^2t^2\right)}\right)\times\left[1-erf\left(\frac{\sigma}{v_e t\sqrt{2\left(\sigma^2+{v_e}^2t^2\right)}}x\right)\right]\end{aligned} \tag{S5}$$

where *erf*(*x*) is the error function. Without the junction, the hole distribution would simply require replacing $v_e$ by $v_h$ and removing the error function. Instead, due to the presence of the junction, we have

$$\rho_h^p(x,y;t)=\frac{N_p}{\pi\left(\sigma^2+{v_h}^2t^2\right)}\exp\left(-\frac{x^2+y^2}{2\left(\sigma^2+{v_h}^2t^2\right)}\right)\times\eta(-x). \tag{S6}$$

Figure S4 shows the cross-section cut of the electron density (red) and hole density (blue) profiles, and their superposition (green) along the x-axis, where the gating effect is clear.

A similar analysis can be provided for carriers in the n-type region. Holes photoexcited initially in n-type can travel into p-type and pass through the gate. Therefore, one has,

$$\begin{aligned}\rho_h^n(x,y;t)&=\int_{-\infty}^{\infty}dv_x\int_{-\infty}^{\infty}dv_y\,f_h(v_x,v_y)\rho_h^n(x-v_xt,y-v_yt)\\&=\frac{N_n}{2\pi\left(\sigma^2+{v_h}^2t^2\right)}\exp\left(-\frac{x^2+y^2}{2\left(\sigma^2+{v_h}^2t^2\right)}\right)\times\left[1+erf\left(\frac{\sigma}{v_ht\sqrt{2\left(\sigma^2+{v_h}^2t^2\right)}}x\right)\right].\end{aligned} \tag{S7}$$

Electrons initially moving toward the junction, however, will encounter the gate and be stopped. As a consequence, we have

$$\rho_e^n(x,y;t)=\frac{N_n}{\pi\left(\sigma^2+{v_e}^2t^2\right)}\exp\left(-\frac{x^2+y^2}{2\left(\sigma^2+{v_e}^2t^2\right)}\right)\times\eta(x). \tag{S8}$$

The cross-section cut of the electron density (red) and hole density (blue) profiles and their sum (pink) along the x-axis are shown in fig. S5.

Effect of lattice and velocity change

The effective time constant $\tau_{e-ph}$ for cooling of hot carriers through the lattice is inversely proportional to the electron-phonon coupling constant as well as the specific heat of carriers. Since the specific heat increases linearly with electron density and temperature, the effective cooling time is not formally constant but can increase significantly at high laser fluences. In our experiments with 515 nm light (2.41 eV, or ≈1.3 eV in excess of the bandgap), we expect excited carriers to initially have temperatures ~$10^4$ K. In addition, increased screening effects due to greater charge carrier density can also lengthen the effective cooling time.

While for low-temperature distributions $\tau_{e-ph}$ is approximately 240 fs for a single scattering event, the associated half-life of temperature decay is ~2 ps (*22*). It has been shown that the effective time constant for a single electron-phonon coupling event can increase from 240 fs to the picosecond scale due to high population density which similarly increases the half-life (*23*,*24*). Our simulations show that for an effective temperature decay half-life of only 5 ps, carrier separation over tens of microns is still present, though it is less extreme than in the fully-ballistic case. Figure S6 depicts the images at four different times, using the closed form equations S5-8 (modified to include velocity decay). The figure clearly indicates that when the lattice energy (and velocity) drops in 10 ps, the observed contrast and spatial extent are still robust.

Further, near the surface, the termination of the periodic structure results in bond softening and a longer electron-phonon coupling time constant. Figure S7 shows charge separation from the surface into the depth of the junction, assuming a coupling constant of 10 ps at the surface with a decay constant of 5 nm into the bulk. Because this effect is isolated near the surface, only surface-sensitive techniques such as SUEM will be able to probe the resulting dynamics.

Simulations

Numerical simulations incorporate certain considerations which, for simplicity, were not included in obtaining the closed form formulae. In the simulations, carriers are accelerated/decelerated when they encounter the junction. Further, the junction is not impassable, and the decelerated carriers may cross it if they have sufficient kinetic energy. The inclusion of surface effects in the simulations was considered but found unnecessary to describe the dynamics. The results of these simulations are provided in the main text in Fig. 3 and 4 which show snapshots of charge density and electric potential after 20 ps.

While +20 ps was chosen for the snapshots, further simulations show that transport continues toward a maximum at ~80 ps. Figure S8 plots the net electron density transported into n-type, integrated from $x$ = 0 to 50 μm from the junction. As was the case in the experiment, the transported charges continue to build excess density for ~80 ps. The growth rate of the signal at short times is $\sim v_e / \sqrt{2\sigma}$, and its proportionality to the averaged thermal electron velocity indicates ballistic electrons transporting from p-type into n-type. Further, one can estimate the signal growth rate of hot electrons ~$1.5\times10^4$ K by fitting the increase of the signal by exponential growth, which results in a time constant ~20 ps. This is also in excellent agreement with the experiment, for which the signals increased with a time constant of 15-25 ps (electrons in n-type) and 30-45 ps (holes in p-type), depending on the region of integration.

Asymmetric excitation: p-type vs. n-type

Because of the difference in doping levels between n-type and p-type, we must consider the effect of asymmetric excitation between the two. High doping in p-type reduces the bandgap (*20*) and consequently increases the absorption cross section. Thus, we introduced the asymmetry

parameter $\mu$ in the simulation which is defined as $\mu \equiv N_n / N_p$ : $\mu = 0$ refers to excitation solely on p-type, while $\mu = 1$ refers to fully symmetric excitation.

Following the calculations for charge density as presented in Fig. 3 (main text), Fig. S9 shows the effect of asymmetric excitation on the electric potential distortions for $\mu = 0$ (A), $\mu = 0.2$ (B) and $\mu = 1$ (C). By combining the charge density and electric potential maps, we obtained the SUEM maps shown in S9D-F, which simulate the measured contrast images. While an initially symmetric distribution leads to increased charge separation, the spatial extent of all calculations spans tens of microns in agreement with our experimental observations.

Effect of beam placement

As briefly mentioned in the main text and shown in Fig. 2C, the apparent "bending" of the junction into p-type is consistent with asymmetric beam placement with the center of the laser spot being placed slightly into n-type. Figure S10 shows a 1-D calculation of the electric potential after 20 ps when the initial excited population is centered 15 μm into n-type (an exaggeration of misalignment). The potential continues to be positive into p-type, resulting from excess electron density affecting the boundary; this behavior accounts for the "bending" seen in Fig. 2C.

Recombination dynamics

Analysis was carried out on dynamic sets which were obtained by combining images recorded at different time delays. The transients were extracted by integrating over the spatial regions shown in fig. S3. Figure S11 shows the transients (contrast versus time) after normalization to the peak contrast, as shown systematically in the figure for the same fluence and region.

The initial rise in n-type (regions I, II) is largely independent of increased fluence. A similar observation is made near the junction in p-type (region III) where the dynamics begins with a positive contrast close to time zero which is later overcome by negative contrast. This suggests that upon optical excitation, p-type behaves similar to controlled p-type without the junction (Fig. 2B in the main text) by showing positive contrast, but the excited carriers are quickly transported across the junction, resulting in negative contrast. Away from the junction in p-type (region IV), this rate reduces at lower fluences.

A stronger example of fluence-dependent dynamics is observed in the carrier relaxation regime in the transient. As an example, electrons are majority carriers in n-type, so their recombination is inherently slow; thus, they energetically prefer to return to p-type where they become minority carriers and recombine with abundant holes. The transients clearly show, for all regions, that the relaxation toward equilibrium occurs more quickly at higher fluences. In fact, at 0.16 $mJ/cm^2$ fluence, the decays essentially plateau within the experimental timescale. The transients suggest that the recombination dynamics are significantly influenced by the number of displaced carriers; specifically, as the system is removed further from equilibrium by larger fluences, recombination is increasingly facilitated.

**Movie and Figure Captions**

**Movie S1.** Displaced charge carriers at 0.16 mJ/cm$^2$ fluence. Following transport, charges remain built up primarily near the junction, while some recombination occurs. Brightness and darkness correspond to electron and hole densities, respectively.

**Movie S2.** Displaced charge carriers at 0.64 mJ/cm$^2$ fluence. As in the case of 0.16 mJ/cm$^2$ fluence, charges gather primarily near the junction (though with greater spatial extent than at lower fluence). Recombination occurs at a comparatively faster rate as electrons return toward the p-type silicon (bottom of screen). A slight bending of the junction can be observed as the potential landscape becomes distorted by the presence of a dynamic bias voltage due to the displaced charges.

**Movie S3.** Displaced charge carriers at 1.28 mJ/cm$^2$ fluence. Due to the large number of displaced charges, the spatial extent is again increased in comparison to lower fluences, though again, displaced carriers generally gather near the junction. Following transport, the junction is distinctly bent as electrons flow into the p-type silicon to recombine.

**Fig. S1.** Schematic of the electronic band diagram in the silicon p-n junction used for this study.

**Fig. S2.** SEM images of a typical surface chosen for SUEM measurements. Surfaces with low roughness were used for this study to avoid interruption in surface carrier diffusion.

**Fig. S3.** (**A**) An unprocessed SUEM image recorded for the p-n junction prior to laser excitation (-680 ps). The dotted ellipse represents the laser beam placement at the junction. The dotted rectangles highlight the regions for which the analysis is presented in fig. S11. (**B**) The contrast image (processed) of the same region +80 ps after optical excitation.

**Fig. S4.** Cross sections of charge density from the p-type layer. Integrating the velocity distributions of charges which originate in p-type results in transport across the junction covering tens of microns. Electrons (red) are transported across the junction, while holes (blue) are blocked, resulting in the net distribution (green).

**Fig. S5.** Cross sections of charge density from the n-type layer. Electrons (red) are reflected by the junction, while holes (blue) are transported into p-type. Their sum (green) illustrates the spatial extent of the net transport.

**Fig. S6.** Simulation of transport with 10 ps temperature decay. Modifying Eq. S5-S8 to include the time-dependent velocity results in transport over tens of microns, similar to the fully-ballistic treatment. Net charge densities are presented for 20 ps (A), 40 ps (B), 60 ps (C), and 80 ps (D).

**Fig. S7.** Charge separation from the surface into the depth of the p-n junction. The graph indicates that charge separation is more pronounced near the surface where the distortion in the lattice results in reduced electron-phonon coupling and thus a longer ballistic lifetime of excited carriers.

**Fig. S8.** Integrated electron density growth in n-type as a function of time. While the majority of transport (presented for electrons transporting from p-type to n-type) occurs within the first ~25 ps, the signal continues to increase toward a peak around 80 ps. Both the initial rate and total time to complete transport mirror the experimental observation.

**Fig. S9.** The effect of asymmetric excitation on the electric potential distortions for $\mu = 0$ (A), $\mu = 0.2$ (B) and $\mu = 1$ (C). The estimated SEM maps (D-F) were obtained by combining the charge density and electric potential maps, which simulate the distortion in the experimentally measured

contrast images. The scale of the normalized density when multiplied by $N_p$, which is $10^9$ e-h pairs, gives the actual density.

**Fig. S10.** 1-D calculation of the electron energy after 20 ps when the initial excited population is centered 15 μm into n-type. The energy continues to be positive into p-type, resulting from excess electron density affecting the boundary.

**Fig. S11.** Spectra corresponding to regional dynamics. Spectra were analyzed from the four regions specified in fig. S3: (I) n-type far from the junction, (II) n-type near the junction, (III) p-type near the junction, and (IV) p-type far from the junction. The data (circles: 1.28 mJ/cm$^2$; triangles: 0.64 mJ/cm$^2$; diamonds: 0.16 mJ/cm$^2$) were normalized to unity for clarity, and a mathematical fit (solid line) is included to guide the eye. Primarily relevant is the consistent trend of higher fluences to relax more quickly toward equilibrium due to increased distortion to the intrinsic junction potential.

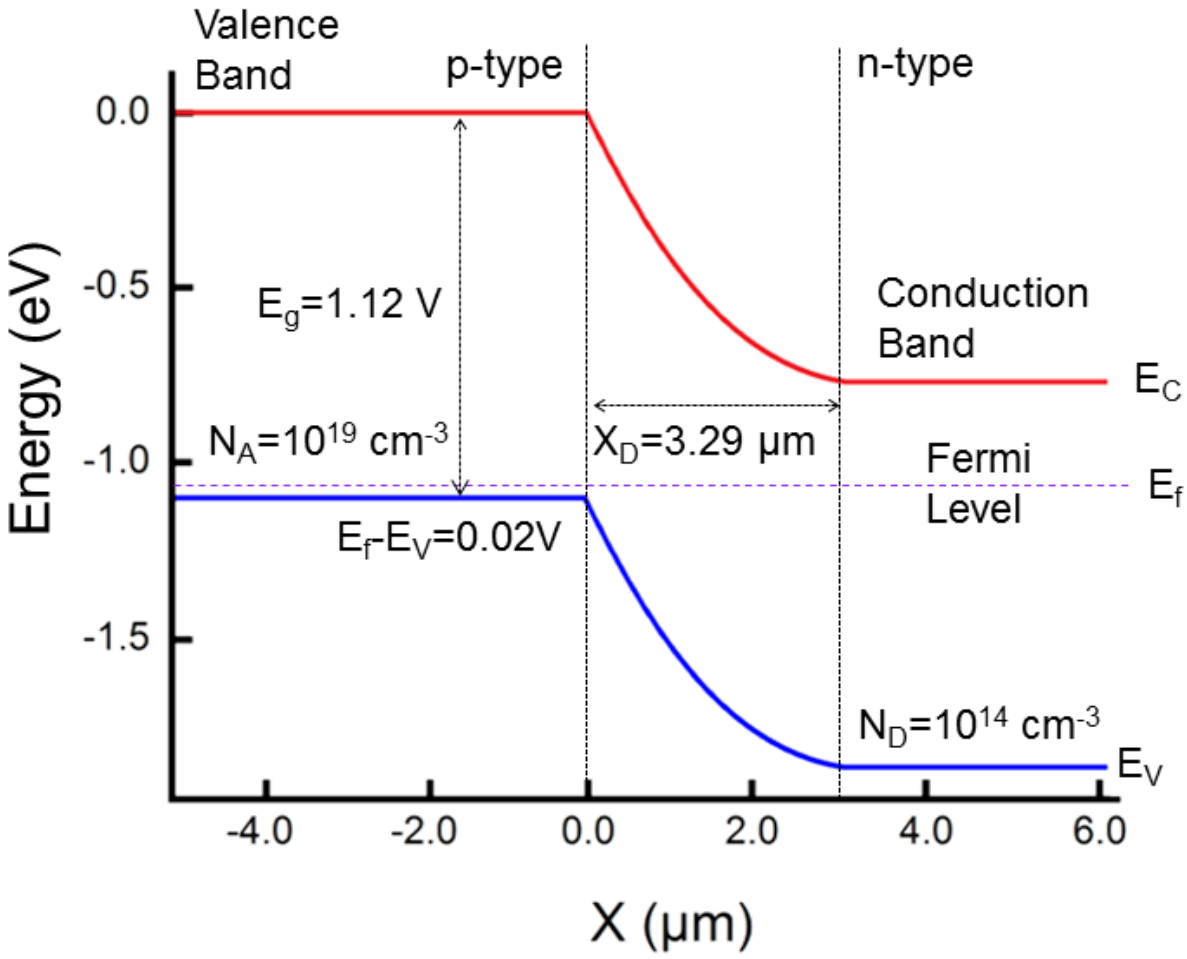


**Fig.S1** E. Najafi, T. D. Scarborough, J. Tang, A. H. Zewail

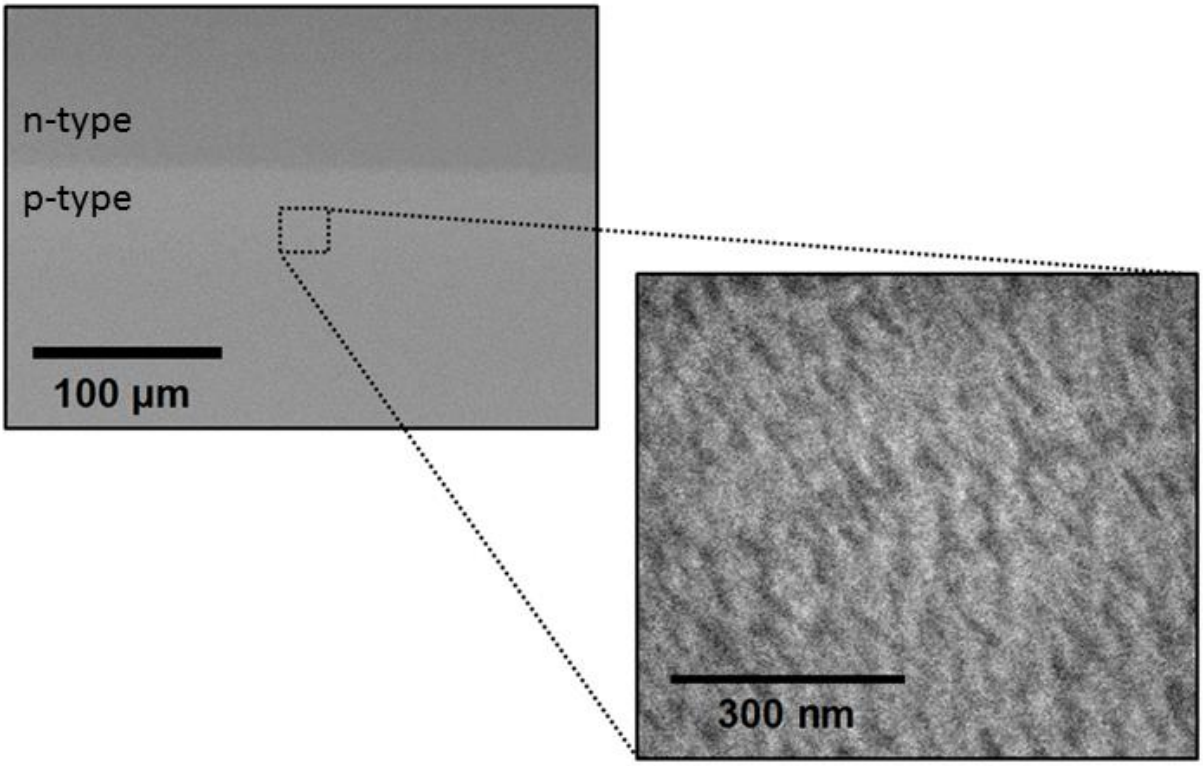


**Fig.S2** E. Najafi, T. D. Scarborough, J. Tang, A. H. Zewail

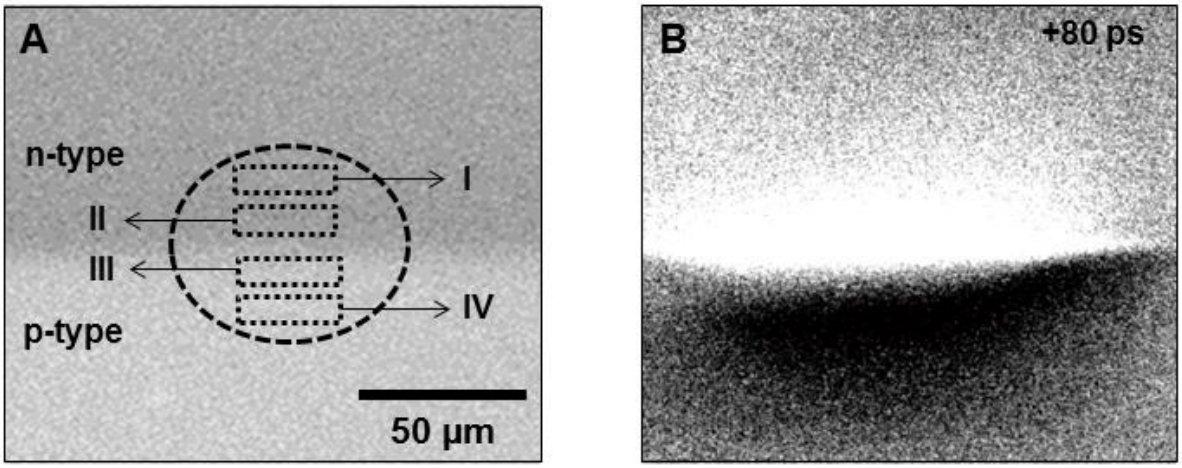


"Raw" Negative Time Image (-680 ps)

Positive Time Contrast Image (+80 ps)

**Fig.S3** E. Najafi, T. D. Scarborough, J. Tang, A. H. Zewail

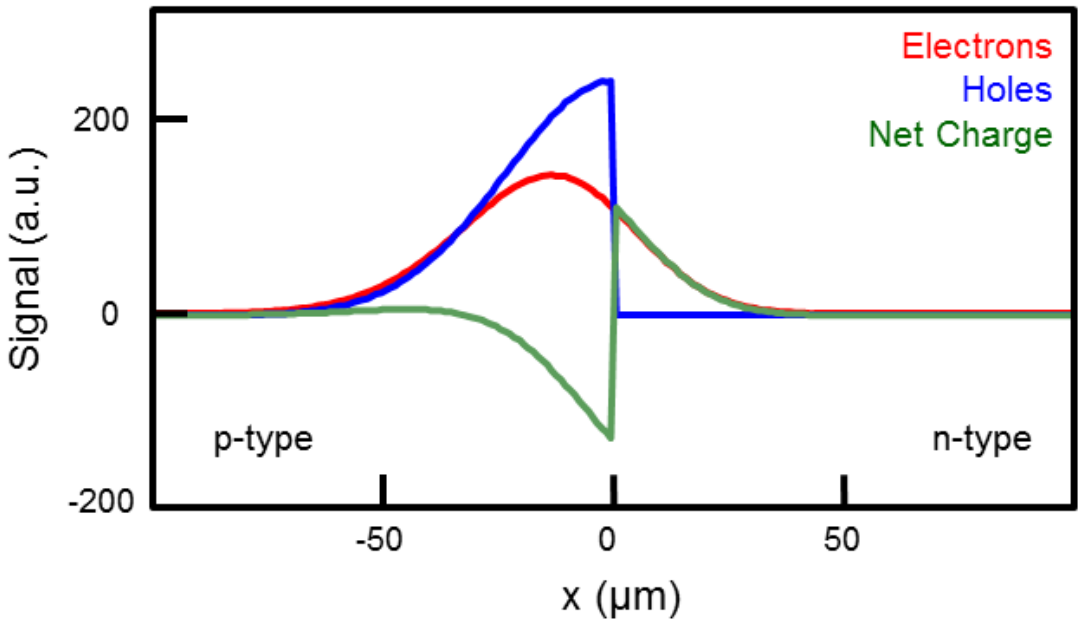


**Fig.S4** E. Najafi, T. D. Scarborough, J. Tang, A. H. Zewail

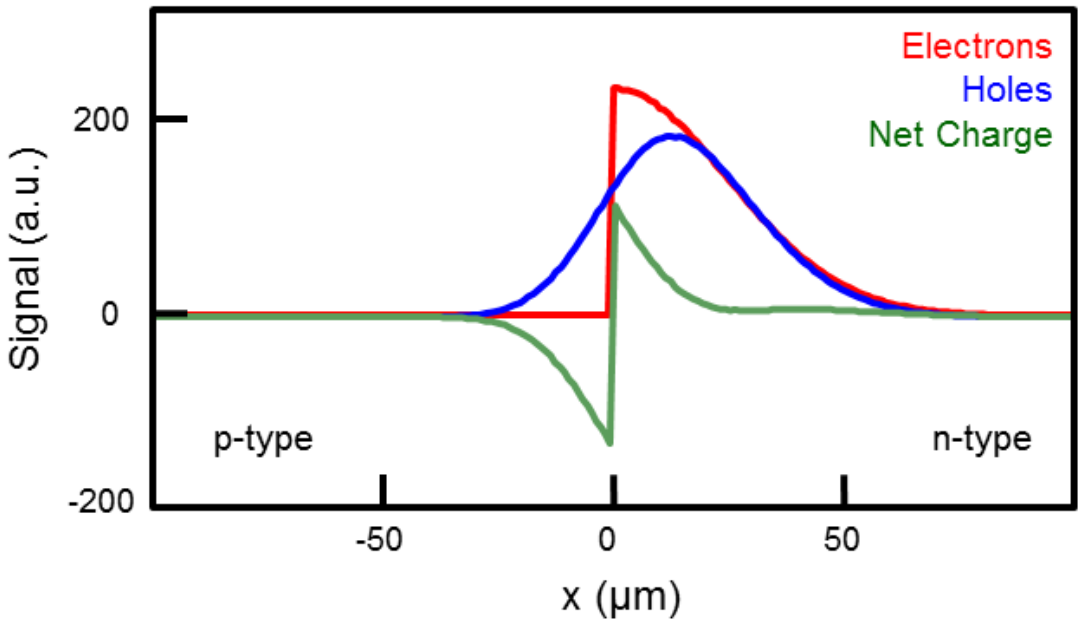


**Fig.S5** E. Najafi, T. D. Scarborough, J. Tang, A. H. Zewail

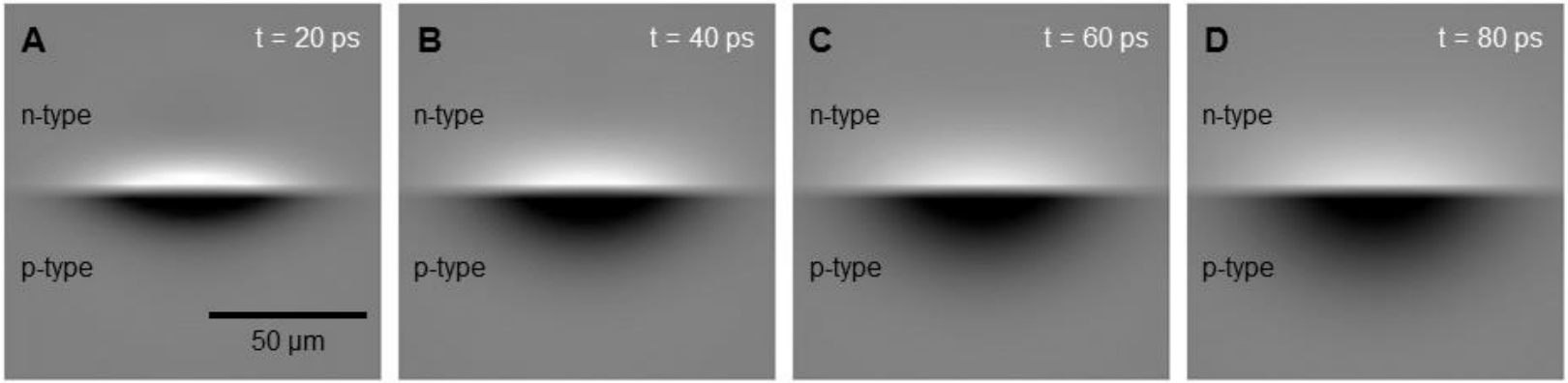


**Fig.S6** E. Najafi, T. D. Scarborough, J. Tang, A. H. Zewail

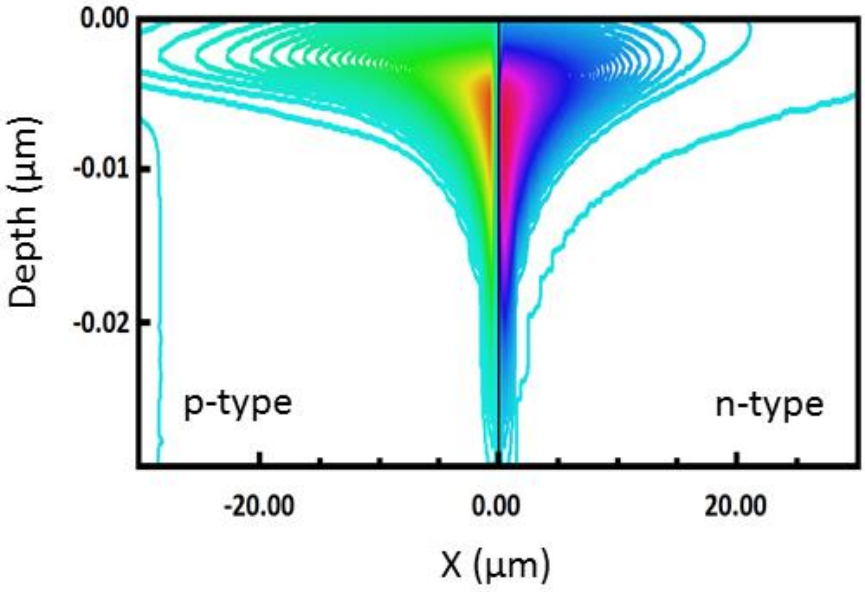


**Fig.S7** E. Najafi, T. D. Scarborough, J. Tang, A. H. Zewail

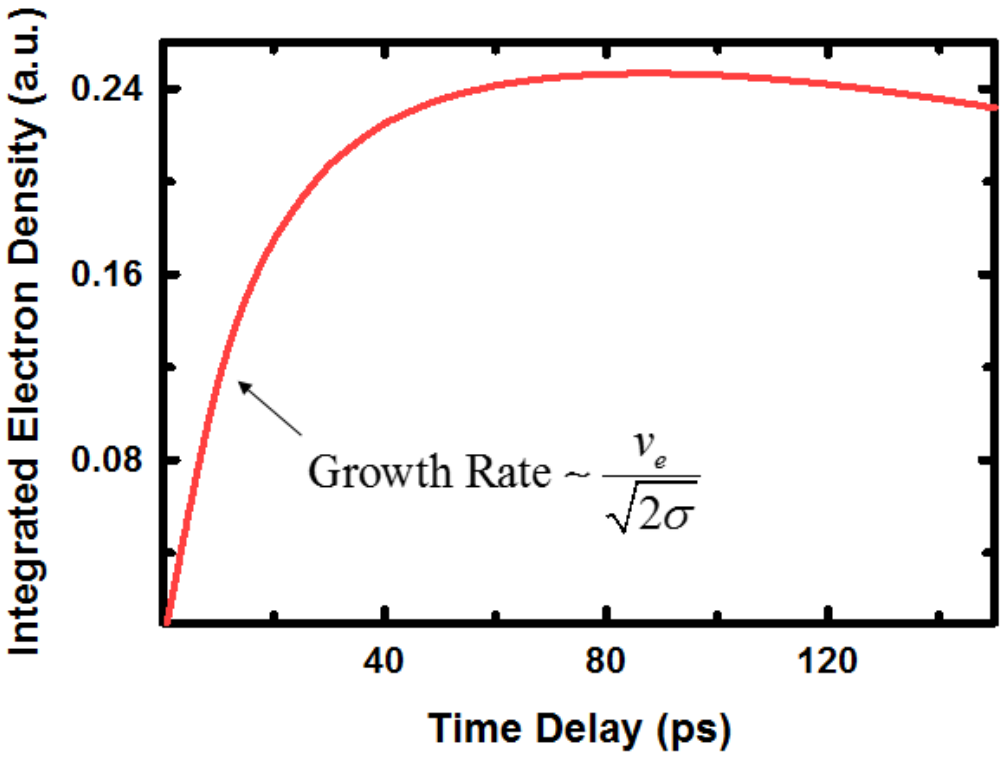


**Fig.S8** E. Najafi, T. D. Scarborough, J. Tang, A. H. Zewail

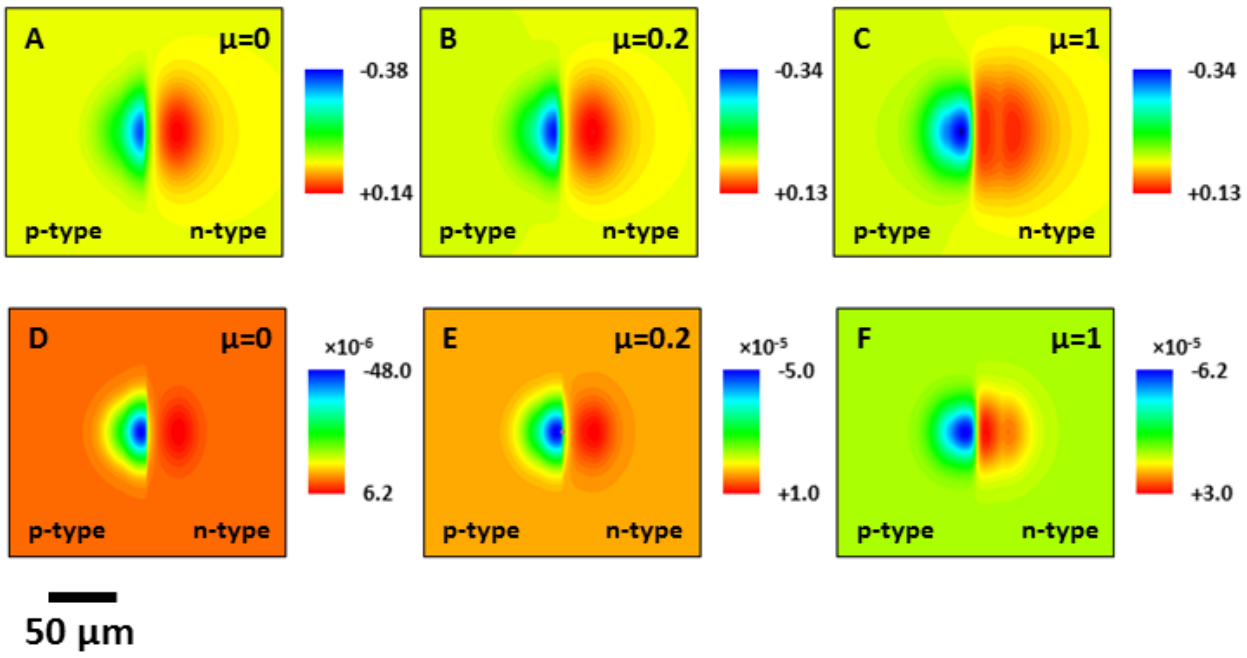


**Fig.S9** E. Najafi, T. D. Scarborough, J. Tang, A. H. Zewail

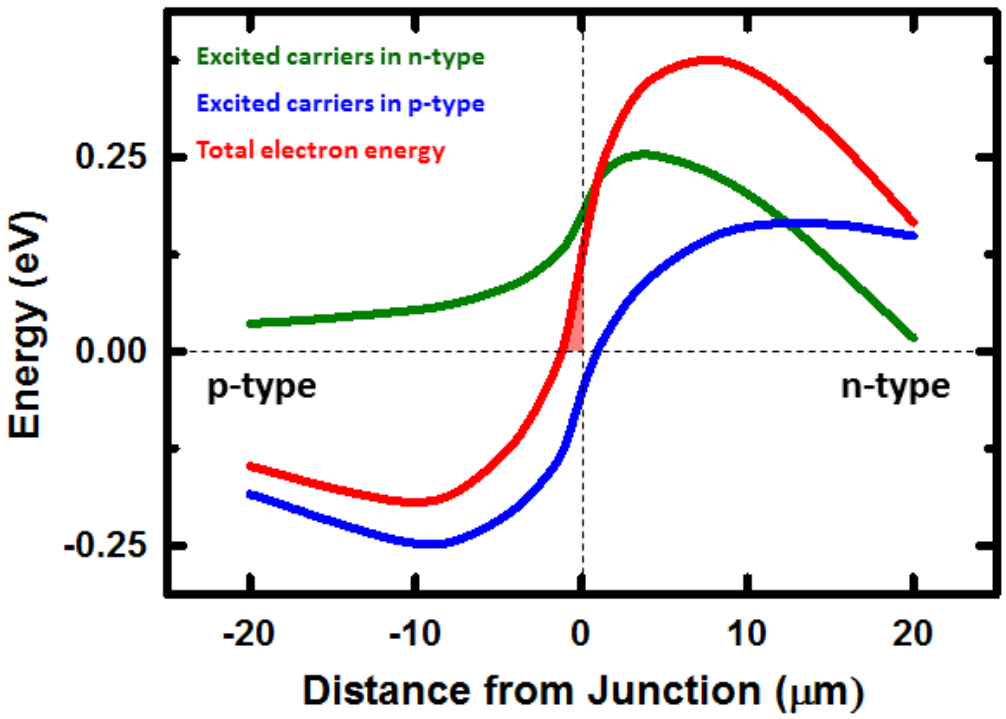


**Fig.S10** E. Najafi, T. D. Scarborough, J. Tang, A. H. Zewail

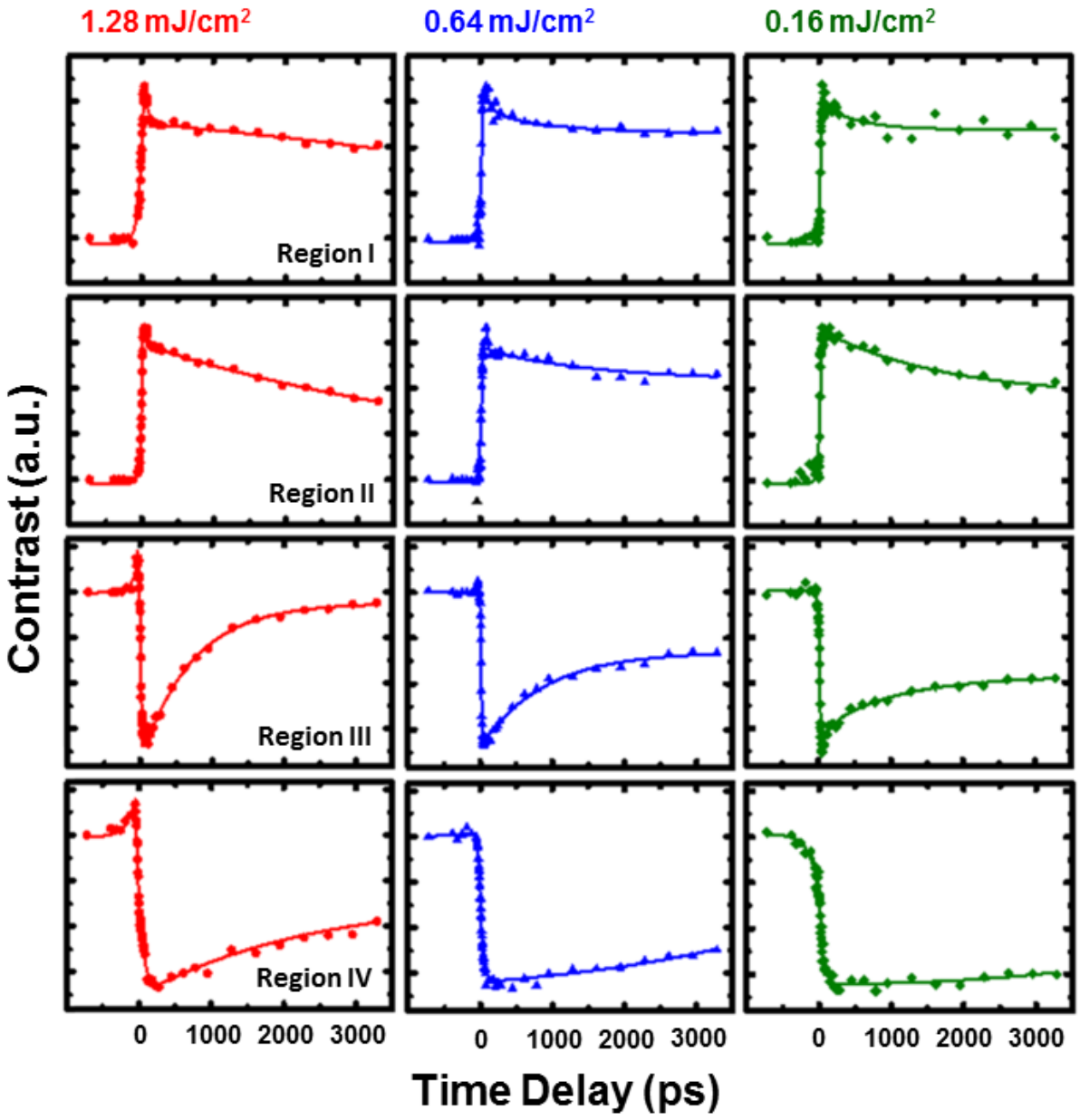


**Fig.S11** E. Najafi, T. D. Scarborough, J. Tang, A. H. Zewail

**References**


1. K.-T. Tsen, Ed., *Ultrafast Dynamical Processes in Semiconductors* (Springer-Verlag, New York, 2004).

2. J. Shah, *Ultrafast Spectroscopy of Semiconductors and Semiconductor Nanostructures* (Springer-Verlag, New York, 1999).

3. D. H. Auston, Ultrafast optoelectronics. *Top. Appl. Phys.* **60**, 183–233 (1993).

4. P. Rodgers Ed, *Nanoscience and Technology: A Collection of Reviews from Nature Journals* (World Scientific, London, 2010).

5. M. Saraniti, U. Ravaioli, *Nonequilibrium Carrier Dynamics in Semiconductors: Proceedings of the 14th Iinternational Conference, July 25-29, 2005, Chicago, USA* (Springer Proceedings in Physics, Berlin, 2006).

6. P. Hommelhoff, M. F. Kling, M. I. Stockman, Ultrafast phenomena on the nanoscale. *Ann. Phys.* **525**, A13–A14 (2013). doi:10.1002/andp.201300709

7. R. P. Prasankumar, P. C. Upadhya, A. J. Taylor, Ultrafast carrier dynamics in semiconductor nanowires. *Phys. Status Solidi B.* **246**, 1973–1995 (2009). doi:10.1002/pssb.200945128

8. A. H. Zewail, Four-dimensional electron microscopy. *Science* **328**, 187–193 (2010). Medline doi:10.1126/science.1166135

9. R. Brunetti, C. Jacoboni, F. Nava, L. Reggiani, G. Bosman, R. J. J. Zijlstra, Diffusion coefficient of electrons in silicon. *J. Appl. Phys.* **52**, 6713–6722 (1981). doi:10.1063/1.328622

10. O. F. Mohammed, D. S. Yang, S. K. Pal, A. H. Zewail, 4D scanning ultrafast electron microscopy: Visualization of materials surface dynamics. *J. Am. Chem. Soc.* **133**, 7708–7711 (2011). Medline doi:10.1021/ja2031322

11. Y. Lin, D. C. Joy, A new examination of secondary electron yield data. *Surf. Interface Anal.* **37**, 895–900 (2005). doi:10.1002/sia.2107

12. S. Schäfer, W. X. Liang, A. H. Zewail, Structural dynamics and transient electric-field effects in ultrafast electron diffraction from surfaces. *Chem. Phys. Lett.* **493**, 11–18 (2010). doi:10.1016/j.cplett.2010.04.049

13. J. Goldstein *et al*., *Scanning Electron Microscopy and X-ray Microanalysis* (Springer, New York, 2007).

14. B. Sapoval, C. Hermann, *Physics of Semiconductors* (Springer-Verlag, New York, 1995).

15. K. W. A. Chee, C. Rodenburg, C. J. Humphreys, High resolution dopant profiling in the SEM, image widths and surface band-bending. *J. Phys. Conf. Ser.* **126**, 012033 (2008). doi:10.1088/1742-6596/126/1/012033

16. K. W. A. Chee, C. Rodenburg, C. J. Humphreys, *Microscopy of Semiconducting Materials 2007*, A. G. Cullis, P. A. Midgley, Eds. (Springer-Verlag, Berlin, 2008).

17. S. L. Elliott, R. F. Broom, C. J. Humphreys, Dopant profiling with the scanning electron microscope - a study of Si. *J. Appl. Phys.* **91**, 9116–9122 (2002). doi:10.1063/1.1476968

18. C. P. Sealy, M. R. Castell, P. R. Wilshaw, Mechanism for secondary electron dopant contrast in the SEM. *J. Electron Microsc.* **49**, 311–321 (2000). Medline doi:10.1093/oxfordjournals.jmicro.a023811

19. G. E. Jellison Jr., F. A. Modine, C. W. White, R. F. Wood, R. T. Young, Optical properties of heavily doped silicon between 1.5 and 4.1 eV. *Phys. Rev. Lett.* **46**, 1414–1417 (1981). doi:10.1103/PhysRevLett.46.1414

20. J. A. Wagner, J. A. del Alamo, Band-gap narrowing in heavily doped silicon: A comparison of optical and electrical data. *J. Appl. Phys.* **63**, 425–429 (1988). doi:10.1063/1.340257

21. D. K. Schroder, Carrier lifetimes in silicon. *IEEE Trans. Electron. Dev.* **44**, 160–170 (1997). doi:10.1109/16.554806

22. D. S. Yang, N. Gedik, A. H. Zewail, Ultrafast electron crystallography. 1. nonequilibrium dynamics of nanometer-scale structures. *J. Phys. Chem. C* **111**, 4889–4919 (2007). doi:10.1021/jp067466+

23. T. Sjodin, H. Petek, H. L. Dai, Ultrafast carrier dynamics in silicon: A two-color transient reflection grating study on a (111) surface. *Phys. Rev. Lett.* **81**, 5664–5667 (1998). doi:10.1103/PhysRevLett.81.5664

24. T. Sjodin, C. M. Li, H. Petek, H. L. Dai, Ultrafast transient grating scattering studies of carrier dynamics at a silicon surface. *Chem. Phys.* **251**, 205–213 (2000). doi:10.1016/S0301-0104(99)00365-1